International Journal of Minerals, Metallurgy and Materials
Volume 30, Number 4, April 2023, Page 697
https://doi.org/10.1007/s12613-021-2371-6

Effects of microstructure characteristics on the tensile properties and fracture toughness of TA15 alloy fabricated by hot isostatic pressing

Langping Zhu[1,2,3], *Yu Pan*[1], *Yanjun Liu*[1], *Zhiyu Sun*[2,3], *Xiangning Wang*[2,3], *Hai Nan*[2,3], *Muhammad-Arif Mughal*[4], *Dong Lu*[5], *and Xin Lu*[1]✉

1) Beijing Advanced Innovation Center for Materials Genome Engineering, Institute of Engineering Technology, University of Science and Technology Beijing, Beijing 100083, China
2) AECC Beijing Institute of Aeronautical Materials, Beijing 100095, China
3) Beijing Engineering Research Center of Advanced Titanium Alloy Precision Forming Technology, Beijing 100095, China
4) Institute of Artificial Intelligence, University of Science and Technology Beijing, Beijing 100083, China
5) Sichuan Advanced Metal Material Additive Manufacturing Engineering Technology Research Center, Chengdu Advanced Metal Materials Industry Technology Research Institute Co., Ltd, Chengdu 610300, China
(Received: 8 August 2021; revised: 26 October 2021; accepted: 1 November 2021)

Abstract: Powder hot isostatic pressing (HIP) is an effective method to achieve near-net-shape manufacturing of high-quality complex thin-walled titanium alloy parts, and it has received extensive attention in recent years. However, there are few reports about the microstructure characteristics on the strengthening and toughening mechanisms of powder hot isostatic pressed (HIPed) titanium alloys. Therefore, TA15 powder was prepared into alloy by HIP approach, which was used to explore the microstructure characteristics at different HIP temperatures and the corresponding tensile properties and fracture toughness. Results show that the fabricated alloy has a "basket-like structure" when the HIP temperature is below 950°C, consisting of lath clusters and surrounding small equiaxed grains belts. When the HIP temperature is higher than 950°C, the microstructure gradually transforms into the Widmanstatten structure, accompanied by a significant increase in grain size. The tensile strength and elongation are reduced from 948 MPa and 17.3% for the 910°C specimen to 861 MPa and 10% for the 970°C specimen. The corresponding tensile fracture mode changes from transcrystalline plastic fracture to mixed fracture including intercrystalline cleavage. The fracture toughness of the specimens increases from 82.64 MPa·m$^{1/2}$ for the 910°C specimen to 140.18 MPa·m$^{1/2}$ for the 970°C specimen. Specimens below 950°C tend to form holes due to the prior particle boundaries (PPBs), which is not conducive to toughening. Specimens above 950°C have high fracture toughness due to the crack deflection, crack branching, and shear plastic deformation of the Widmanstatten structure. This study provides a valid reference for the development of powder HIPed titanium alloy.

Keywords: powder; titanium alloy; hot isostatic pressing; strength; fracture toughness

1. Introduction

With the rapid development of modern aerospace technology, higher requirements are put forward for new structural materials in terms of light weight, high strength, and heat resistance. Therefore, high-performance thin-walled complex titanium alloys have a wide range of application scenarios, such as air intakes, thin-walled nacelles, complex housings [1–2], and other components. However, this also brings unprecedented challenges to the corresponding titanium alloy forming and manufacturing technology. Traditional cast titanium alloys have poor structure uniformity and are easy to introduce metallurgical defects [3–4]. Additionally, forging technology is difficult to achieve the overall formation of thin-walled complex parts and multi-section riveting or welding. This leads to poor overall rigidity and surface flatness of the parts, which cannot meet the application requirements of aerospace equipment.

In recent years, hot isostatic pressing (HIP) near net forming technology (NNS-HIP) offers an attractive near-net shaping technology for fabricating high-quality thin-walled complex titanium alloy components [5], which has received more and more attention. Furthermore, high reliability is the constant pursuit of key components. Under the guidance of conventional strength theory, many studies have focused on higher strength titanium alloys, such as the use of finer structures [6] or the introduction of reinforcing materials [7–8] to reduce weight by reducing the cross-sectional area of parts. Traditional design theory treats the material as a continuous uniform body. However, many accidents in engineering applications indicate that the fracture originates from defects or cracks in the parts. Therefore, in order to reduce the risk of catastrophic failure of components during use [9], the toughness of materials, that is, the ability to resist fracture, has re-

✉ Corresponding author: Xin Lu E-mail: luxin@ustb.edu.cn

ceived more and more attention. Therefore, strength and toughness have become important indicators to test the overall materials performance. At present, the strengthening and toughening of metal materials has two theories. The first is fine-grain strengthening and toughening. Due to the disordered arrangement of the grain boundary atoms, the resistance to deformation is greater than that in grain. The smaller the grain, the larger the grain boundary area, and the more the energy consumed by the crack tip propagation, resulting in a greater strengthening and toughening effect [10]. The second is the strengthening and toughening of composite structures. In a composite structure formed by alternating high-strength matrix and high-plasticity reinforcement, the ductile phase can play an important role in improving toughness. When crack in the high-strength matrix propagates to the ductile phase, the ductile phase dominates the plastic deformation and weakens the local stress concentration (passivation) at the crack tip [11], thereby preventing the crack from further propagation ahead. As a result, the strength and toughness of the material are improved. However, traditional powder metallurgy processes often introduce residual holes or impurity pollution [12–13], resulting in low reliability and thereby limiting their application. In recent years, more and more studies have shown that the powder HIP process can eliminate the holes and inclusions defects, obtaining alloy with high relative density. As a result, its mechanical properties are close to those of cast and forged titanium alloys. Wang *et al.* [14] fabricated a powder hot isostatic pressed (HIPed) Ti–6Al–4V alloy with a fine and uniform basket structure. The fracture toughness and tensile strength reached 105.7 $MPa \cdot m^{1/2}$ and 920–960 MPa, respectively. Hidalgo *et al.* [15] also confirmed that the strength and toughness of powder HIPed Ti–6Al–4V can reach or exceed the strength and toughness of forged alloys. An in-depth understanding of the strengthening and toughening mechanisms of powder titanium alloys is of great significance for mastering the material service reliability and promoting its application. Many studies have shown that the lamellar structure in titanium alloys is an important way to improve the toughness. For example, the cast Ti–6Al–4V and TA15 alloys have a coarse Widmanstatten structure, and the corresponding fracture toughness is much higher than the duplex structure and equiaxed structure obtained by forging. For this lath cluster structure, crack branching and deflection will occur when the crack tip meets the ductile α laths, which increasing the tortuosity of the crack propagation path and the crack surface area [16–20]. Nevertheless, the introduction of coarse lamellar structure reduces the strength and plasticity. The toughness of the Ti–6Al–4V alloy coarse lamellar structure is 100% higher than that of the equiaxed structure, but its yield strength and elongation are reduced by 5% and 50%, respectively [21]. At present, there are few reports about the strengthening and toughening mechanisms of powder HIPed titanium alloys. Therefore, it is of great significance to investigate the microstructure characteristics on the strengthening and toughening mechanisms of powder HIPed titanium alloys.

In this work, we attempt to prepare high-performance TA15 alloy by powder HIP technology. The microstructure characteristics at different HIP temperatures and the corresponding tensile properties and fracture toughness were systematically studied. This work is expected to promote the development of powder HIPed TA15 alloys.

2. Experimental

Spherical pre-alloyed TA15 powder (supplied by Sino-Euro Co., Ltd) was prepared by rotating electrode atomization method. Carbon steel capsules with diameter of 140 mm and height of 150 mm were prepared. After the capsules were filled with powder, vacuum thermal degassing was performed with vacuum degree of 1×10^{-3} Pa, heating temperature of 550°C, and holding time of 24 h. Finally, the capsules were HIPed in the HIPEX400 HIP equipment with pressure of 120 MPa and holding time of 3 h. According to report [22], the commonly used HIP temperature of titanium alloy powder is 930°C. Thus, the testing HIP temperatures were selected at 4 temperature points equally spaced from 910 to 970°C, namely 910, 930, 950, and 970°C.

Particle size distribution of powder was measured by Zetasizer Nano ZS laser particle size analyzer, and phase composition was analyzed by X-ray diffractometer (XRD; Dmax-RB, Cu K_α, λ = 0.15406 nm). According to the sampling position shown in Fig. 1, the test specimens were obtained by machining in the HIPed capsules. Struers metallographic preparation system was used to prepare metallographic specimens, and the corrosion solution was Kroll's reagent (3vol%HF + 5vol%HNO_3 + 92vol%H_2O). The microstructure and fracture morphology were observed by Zeiss 3M optical microscope (OM) and Zeiss SUPRA55 field emission scanning electron microscope (SEM). Image-Pro Plus software was used to calculate the grain size. The phase

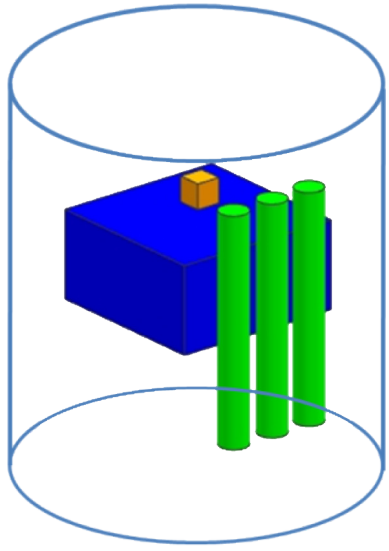

Fig. 1. Schematic diagram of the sampling location in HIPed capsule. Yellow represents metallographic specimens, green represents tensile specimens, and blue represents fracture toughness specimens.

transition point (T_β) of the powder HIPed alloy was measured with the DSC25 thermal analyzer. According to the standard HB 6623.1-1992, T_β is defined as the peak value of the first derivative of the differential thermal curve. The specimen was placed in an Al_2O_3 crucible and protected by flowing high-purity argon in the experiment. Two specimens were tested to reduce the error. The room temperature tensile test was finished by AVIC Touchstone Testing Innovation (Dachang) Corporation. It was carried out on the Instron 5569R electronic universal testing machine according to the GB/T 228.1-2010 standard. The test specimen size was M12 × 71 mm, and the tensile gauge length was ϕ5 × 25 mm. The loading speed was 0.15 mm/s. Engineering stress–strain curves were obtained, and the stress value of 0.2% residual deformation on the stress–strain curve is regarded as the yield strength. Three specimens were tested in each group, and the results were averaged. The fracture toughness was tested on the MTS-250 kN^{-1} testing machine using the compact tensile method. The width of the specimens was 70 mm and the thickness was 35 mm.

3. Results

3.1. Powder characterisation

The chemical composition of the TA15 alloy powder is shown in Table 1. It can be seen that the oxygen content is only 0.088wt%, and other components also meet the application standard. Fig. 2 shows the powder surface morphology and particle size distribution curve. The powder surface is smooth and the particle size distribution is relatively concentrated (Fig. 2(a)), with no satellite ball powder found. The particle size distribution shown in Fig. 2(b) obeys the normal distribution, with D_{50} = 60.1 μm and D_{90} = 116 μm. From the analysis of powder internal microstructure (Fig. 3(a)) and XRD spectrum (Fig. 3(b)), the powder particles are composed of needle-like α′ phases.

3.2. Microstructure analysis

Fig. 4 shows the microstructure of TA15 alloy HIPed at 910 and 930°C. It can be seen that both specimens show "basket-like structure" of fine lath clusters (Fig. 4(a) and (c)).

Table 1. Chemical composition of the raw TA15 alloy powder wt%

Sample	Ti	Al	Zr	Mo	V	O	N	H	C
GB/T 3620.1	Bal.	5.5–7.1	1.5–2.5	0.5–2.0	0.8–2.5	≤0.15	≤0.05	≤0.015	≤0.08
Tested alloy	Bal.	6.47	2.04	1.51	2.26	0.088	0.005	0.0014	0.007

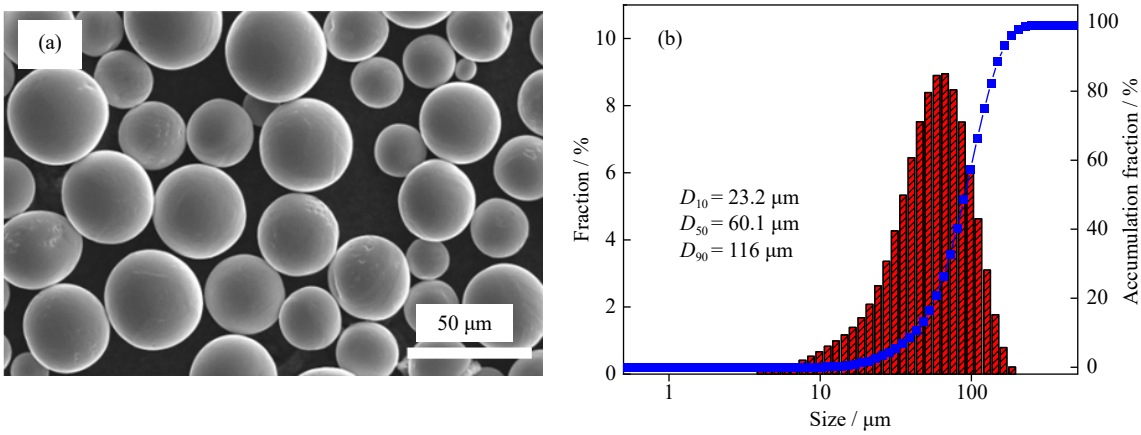

Fig. 2. (a) Surface morphology and (b) particle size distribution curve of the TA15 powder. D_{10}, D_{50}, and D_{90} represent the corresponding particle sizes when the accumulation fractions reach 10%, 50%, and 90%, respectively.

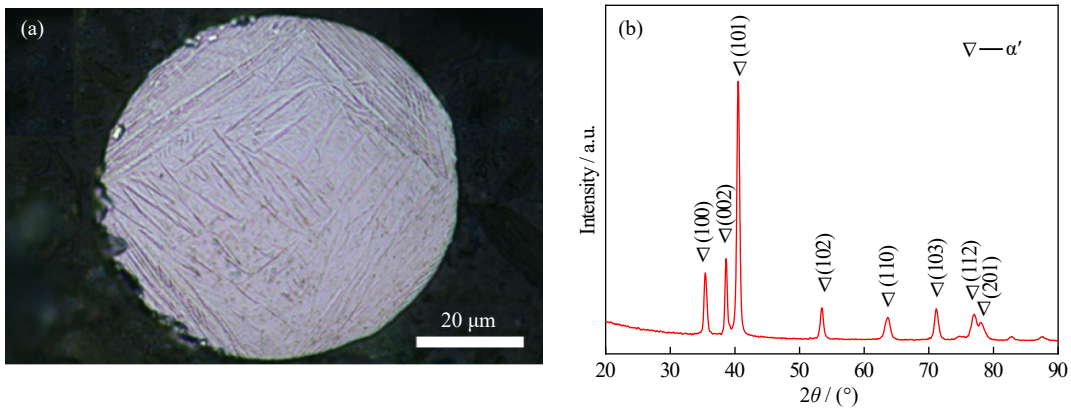

Fig. 3. (a) Powder internal structure and (b) XRD spectrum of the TA15 powder.

Fig. 4(b) and (d) shows that the specimens exhibit a lath structure, and the lath clusters of different orientations are wrapped by a circle of equiaxed grain belts composed of small equiaxed grains, as shown in the area with yellow background. The equiaxed grain belts are composed of equiaxed α grains and a small amount of residual β phase at the edges. Comparing Fig. 4(b) and (d), it can be found that the equiaxed grain belts of the 930°C specimen is wider than those of the 910°C specimen.

Fig. 5 shows the microstructure of the 950°C specimen and the 970°C specimen. It can be seen from Fig. 5(c) that the 970°C specimen is Widmanstatten structure. From Fig. 5(b) and (d), it can be found that there are flat and slender α lath clusters inside the coarse original β grains, and continuous α phase at the grain boundary, which is a typical β transformation structure. In addition, the 950°C specimen has a small amount of equiaxed α phase at the edge of the original β grains, forming "near Widmanstatten structure." Comparing Fig. 5(a) and (c), it can be found that the grains of 970°C specimen are larger than those of the 950°C specimen.

The statistical results of the average lath spacing (W_l) and the volume content of equiaxed grains (V_e) for each specimen are shown in Fig. 6. It can be seen that, compared with the 910°C specimen, the content of equiaxed grains for the 930°C specimen decreased from 4.1% to 3.7%, while the average lath spacing increased from 1.3 to 2.4 μm. With the HIP temperature increase, the content of the equiaxed grain decreases rapidly and disappears when the temperature reaches 950°C. The spacing of α laths tends to increase with the increase of HIP temperature.

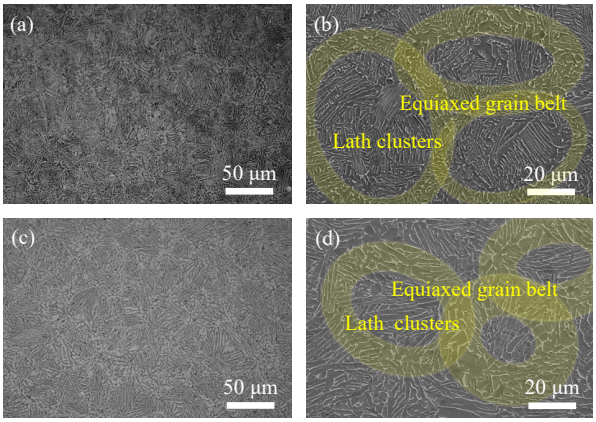

Fig. 4. Microstructure of HIP TA15 alloy at different temperatures: (a) optical image of 910°C alloy; (b) SEM image of 910°C alloy; (c) optical image of 930°C alloy; (d) SEM image of 930°C alloy.

3.3. Tensile properties analysis

The room temperature tensile properties of specimens prepared with different HIP temperatures are showed in Fig. 7. It

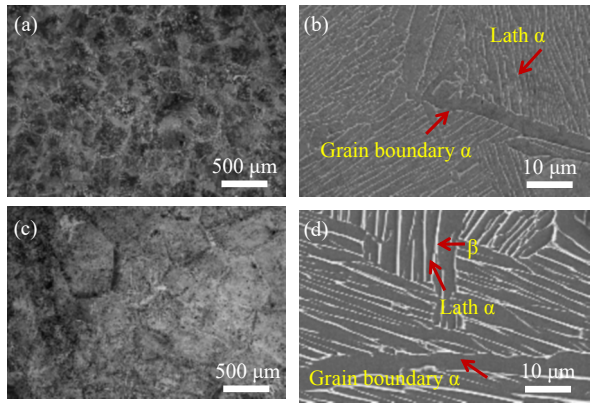

Fig. 5. Microstructure of HIP TA15 alloy at different temperatures: (a) optical image of 950°C alloy; (b) SEM image of 950°C alloy; (c) optical image of 970°C alloy; (d) SEM image of 970°C alloy.

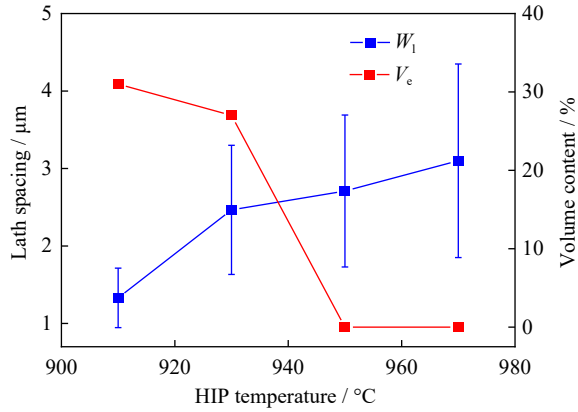

Fig. 6. Variation of lath spacing and volume content of equiaxed grain with different HIP temperatures.

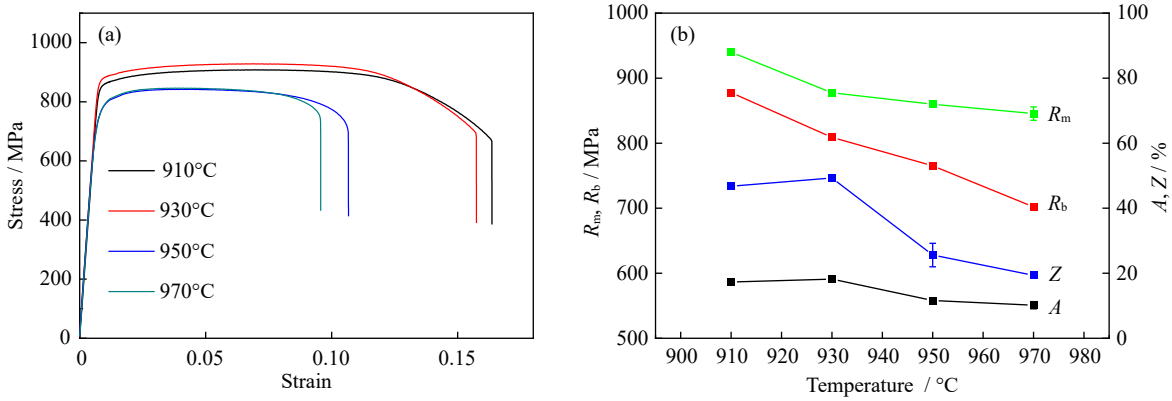

Fig. 7. Tensile properties of specimens at different HIP temperatures: (a) stress–strain curve; (b) curves between ultimate strength (R_m), yield strength (R_b), elongation (A), and shrinkage after breaking (Z) and HIP temperature.

can be seen that as the HIP temperature increases, the strength and elongation of the specimens show a significant downward trend. The tensile strength and yield strength decrease from 948 MPa and 878 MPa for the 910°C specimen to 861 MPa and 762 MPa for the 970°C specimen. Meanwhile, the elongation decreases from 17.3% for the 910°C specimen to 10% for 970°C alloy.

Fig. 8 shows the tensile fracture morphologies of the 910°C specimen. It can be seen from Fig. 8(a) that the specimen has obvious necking and fiber areas. The fiber area is rough and the shear lip is relatively smooth. There are many irregular holes in the fissure fiber area, as shown in Fig. 8(b). Fig. 8(c) shows the fractured cross-sectional structure. The secondary crack is located in the center of the fracture. It can be seen from Fig. 8(d) that the cracks propagate along the prior particle boundaries (PPBs).

The tensile fracture morphologies of the 930°C specimen are shown in Fig. 9. It can be seen from Fig. 9(a) that the macroscopic fracture morphology is consistent with that of 910°C specimen. Fig. 9(b) shows that there are holes formed from PPBs, and the pore size is significantly reduced compared with 910°C specimen. Under high magnification, there are dimples and tearing edges in the fiber zone, seen from Fig. 9(c), and dimples in the shear lip area of the edge, as shown in Fig. 9(d).

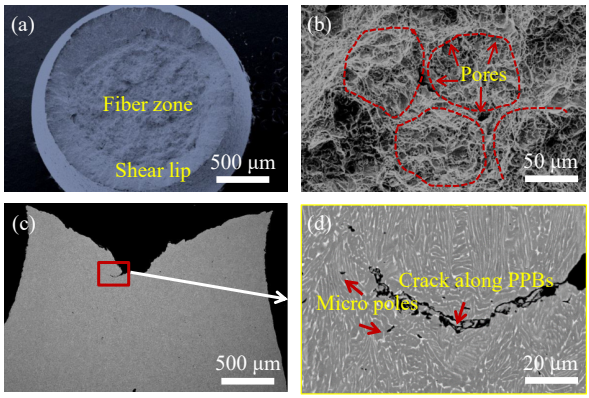

Fig. 8. Tensile fracture morphologies of the 910°C alloy: (a) overall fracture morphology; (b) rough surface of fiber zone; (c) holes distribution in the fiber area; (d) crack along PPBs.

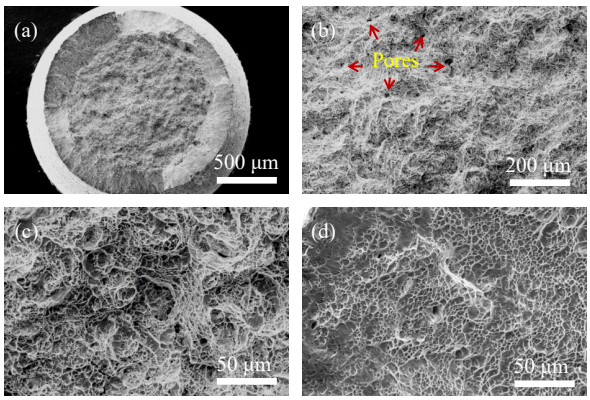

Fig. 9. Tensile fracture morphologies of the 930°C specimen: (a) overall fracture morphology; (b) rough surface of fiber zone; (c) holes distribution in the fiber area; (d) dimples in shear lip zone.

Fig. 10 shows the tensile fracture morphologies of the 950°C specimen. It can be seen from the Fig. 10(a) that the fracture surface is rough and uneven. The cleavage plane is clearly visible, showing the characteristics of transgranular fracture (Fig. 10(b)). The secondary cracks and dimple features are found in Fig. 10(c). In addition, there are tearing edges and dimples on the edges of the fracture (Fig. 10(d)). The entire section shows mixed fracture characteristics.

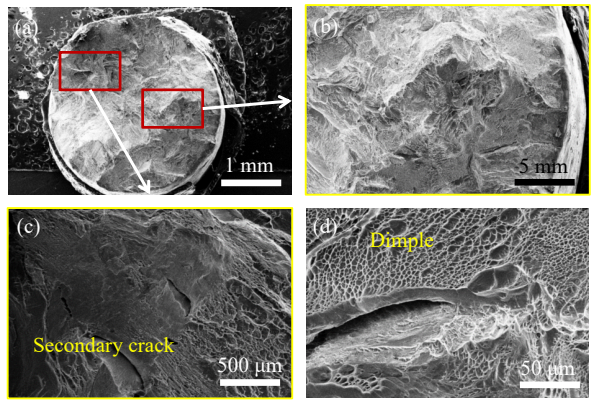

Fig. 10. Tensile fracture morphologies of the 950°C specimen: (a) overall morphology of the fracture; (b) edge morphology of the fracture; (c) secondary crack in the fracture internal area; (d) dimple characteristics.

Fig. 11 shows the tensile fracture morphologies of the 970°C specimen. It can be seen from Fig. 11(a) that there are several large cleavage planes on the cross section. Both the core and the edge of the fracture are shown in Fig. 11(b) and (c). The cleavage planes converge on the grain boundary. Thus, it has the characteristics of intercrystalline cleavage fracture. In addition, under the high magnification structure, the dimple features can be found, as shown in Fig. 11(d). The entire fracture still shows mixed fracture characteristics.

3.4. Fracture toughness analysis

The fracture toughness results of different specimens are shown in Fig. 12. Arranged in ascending order of the HIP

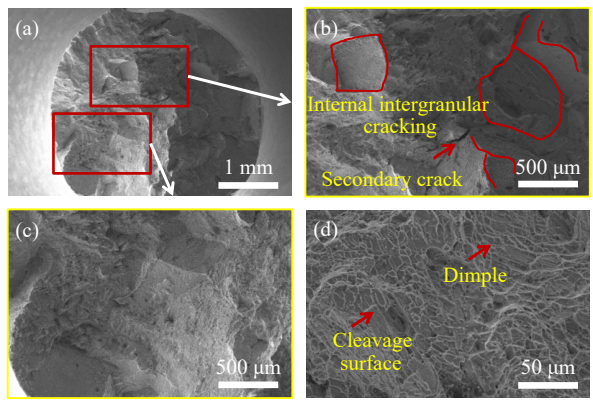

Fig. 11. Tensile fracture morphologies of the 970°C specimen: (a) overall morphology of the cross-section; (b) internal intergranular cracking; (c) intergranular cracking at the edge; (d) cleavage and dimple feature.

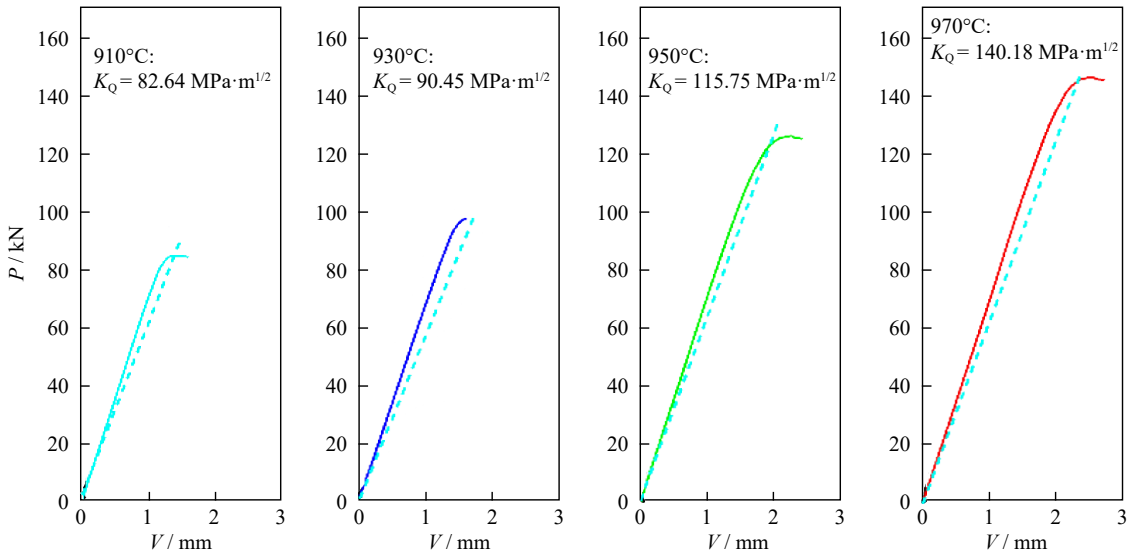

Fig. 12. ***P–V*** **curves of the powder HIPed TA15 alloys prepared at different HIP temperatures.** ***P*** **and** ***V*** **represent the load and the crack opening displacement, respectively.**

temperature of the specimens, the fracture toughness values are 82.64, 90.45, 115.75, and 140.18 MPa·m$^{1/2}$, respectively. The result of the 910°C specimen acquired is K_{IC} (fracture toughness), while the other three results are K_Q (conditional fracture toughness) as they do not meet the condition of Eq. (1). Since all specimens have the same thickness, the fracture toughness values obtained in the test are comparable. It can be seen from the test results that with the increase of the HIP temperature, the fracture toughness value increases gradually.

$$W - a \gg 2.5\left(\frac{K_Q}{\sigma_{0.2}}\right)^2 \tag{1}$$

where W is the width of test specimen, a is the pre-crack length, and $\sigma_{0.2}$ is the yield strength of specimens.

In order to analyze the crack propagation mechanism, the microstructure at the fracture edge of the fracture toughness specimens was observed. Figs. 13 and 14 show the fracture morphologies after fracture toughness test for the 910 and 930°C specimens, respectively. A large number of dimples appear on the fracture surface (Fig. 13(a)), and the laths on the fracture surface had been bent and deformed (Fig. 13(a)). As shown in Fig. 13(b)–(d), there are many holes at the crack edge. It can be seen from Fig. 13(c) that these holes are mainly distributed in the equiaxed grain region formed on the surface of the original powder particles, with a diameter of 10 μm. It is found in Fig. 13(d) that there are many micropores at the crack tip, which are linearly distributed along the flaky β phase. The fracture of the 930°C specimen has similar characteristics with 910°C specimen. It can be seen from Fig. 14(a) that there are secondary cracks on the fracture surface. From Fig. 14(b) and (c), there are many holes on the fracture surface and micropores near the surface. In addition, many micropores are formed in the flaky β phase (Fig. 14(d)).

Fig. 15 shows the morphologies of the fracture toughness fracture edge of the 950°C specimen. It is found from the Fig. 15(a) and (b) that there are secondary cracks in the interior and edge of the original β grains. Fig. 15(c) is an enlarged morphology of the secondary crack in Fig. 15(a). It can be seen that the crack extends along the laths into the grain. After encountering the vertical laths, the crack propagation

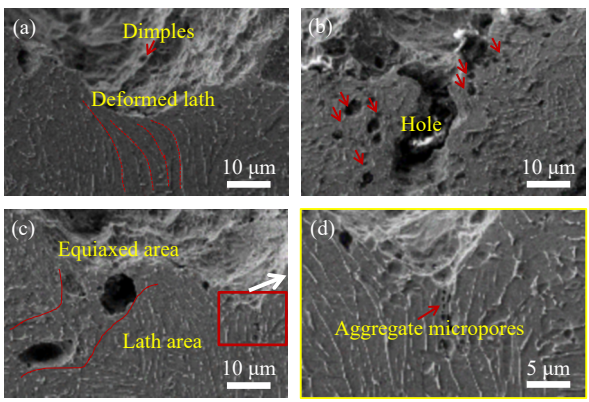

Fig. 13. Fracture morphologies after fracture toughness test for the 910°C specimen: (a) shear deformation of lath; (b) aggregated holes around cracks; (c) porosity in equiaxed grain region; (d) aggregated micropores along β phase.

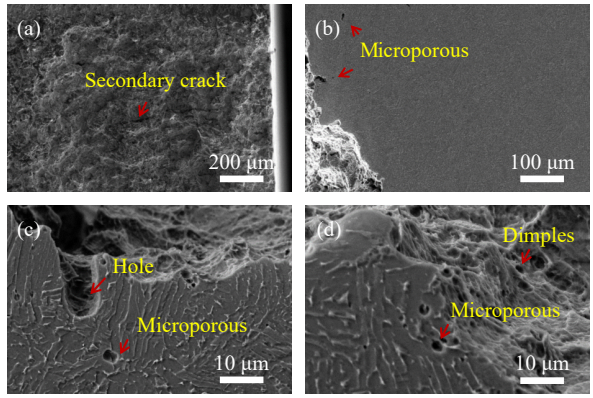

Fig. 14. Fracture morphologies after fracture toughness test for the 930°C specimen: (a) secondary cracks on the fracture surface; (b) scattered micropores near the surface; (c) holes and micropores at the front; (d) micropores on the flaky β phase.

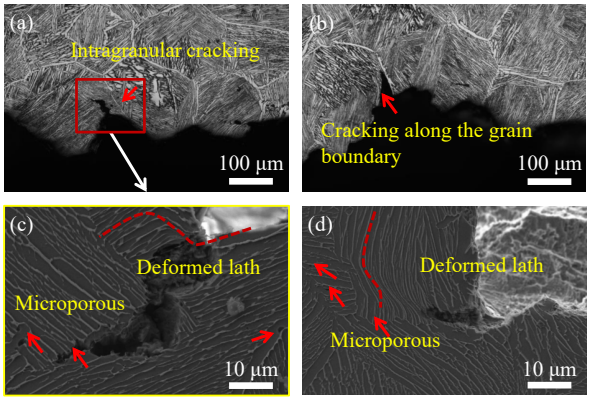

Fig. 15. Fracture morphologies after fracture toughness test of the 950°C specimen: (a) intragranular cracking; (b) cracking along the grain boundary; (c) lath shear deformation and crack propagated along laths; (d) lath shear deformation and dispersive micropores in the front of the crack tip.

direction is deflected. From Fig. 15(c) and (d), the shearing effect of the crack causes the laths to bend and form scattered micropores in the uncracked area at the front edge of the crack tip.

The microstructure near the fracture surface of 970°C spesimen is shown in Fig. 16. In Fig. 16(a), secondary cracks appear in the pre-cracked area. Fig. 16(b) shows that the cracks have branched, forming new cracks parallel to the laths. In Fig. 16(c), the cracks extend perpendicular to the laths, and many scattered micropores are formed around the crack. At the same time, the laths at the front of the crack tip undergo shear deformation. In Fig. 16(d), it can be seen that the fracture has the characteristics of stepped cleavage fracture, indicating that the crack continues to deflect in the process of propagation.

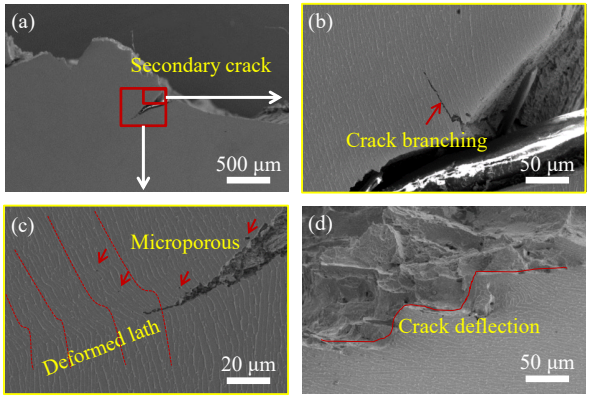

Fig. 16. Fracture morphologies after fracture toughness test of the 970°C specimen: (a) secondary crack; (b) crack branching; (c) lath shear deformation; (d) crack deflection.

4. Discussion

4.1. The effect of microstructure on the strength and plasticity of the alloy

Both the 910°C specimen and the 930°C specimen have fine-grained "basket-like structure" composed of irregular lath clusters and equiaxed grains surrounding the lath clusters (Fig. 4). It can be seen from Fig. 7 that both of them have higher strength and plasticity. The fracture morphologies in Figs. 8 and 9 also show the transgranular plastic fracture characteristics. It proves that their fine-grained structures have a better coordination ability to plastic deformation. In addition, due to the weak bonding force of PPBs, it is easy to debond under tensile stress and form holes, as shown in Figs. 8(b) and 9(b). The crack in Fig. 8(d) indicates that the PPBs provide an important channel for cracks propagation. The results of Cai *et al.* [23] also found that cracks propagate along PPBs. The tendency of cracking along the equiaxed grain region under tensile stress is increased, resulting in a large number of concentrated holes in this area. This phenomenon has been further verified on the fracture toughness test section, as shown in Fig. 13. Guo *et al.* [24] also proved that PPBs can accelerate crack propagation.

The differential scanning calorimetry (DSC) results show that the β transition temperature (T_β) of the powder TA15 alloy specimen is about 969–972°C, as shown in Fig. 17, which is basically consistent with the results of the TA15 ELI titanium alloy reported by Wang *et al.* [25] and Li *et al.* [26]. The alloy has entered the α + β two phases region and close to T_β when the HIP temperature increases to 950°C. As a result, most of the area transforms into β phase, leaving only a small amount of equiaxed α phase at the grain edges. In the subsequent cooling process, the β phase transforms into lath clusters and continuous boundary of α phase, and the equiaxed α phase retained to room temperature, forming "near Widmanstatten structure," as shown in Fig. 5(b). Guo *et al.* [19] also obtained the microstructure characteristics of the original β grains when the HIPed TC4 alloy was heat-treated at a temperature close to T_β. As a result, the alloy transforms into a β single-phase structure at high temperatures. Since the β grains are no longer pinned by the equiaxed α phase, they grow up quickly. After cooling to room temperature, a Widmanstatten structure composed of α laths and residual β phase between the α laths is formed, as shown in Fig. 5(d).

Compared with the low-temperature specimens, the grain sizes of the 950°C and 970°C specimens are significantly larger. Generally speaking, larger crystal grains mean worse plastic deformation coordination performance, and the plastic

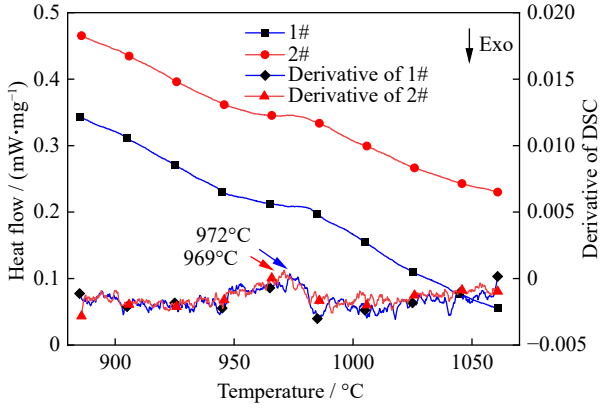

Fig. 17. DSC curves of two powder TA15 alloy specimens.

deformation of the lamellar structure is mainly achieved by the shear bending of the lath, as shown in Figs. 15(d) and 16(c). Cracks can propagate and break along the grain boundaries (Fig. 15(b)), along the laths (Fig. 16(b)), or through the laths (Fig. 16(c)), which is not conducive to improving plasticity. It can be seen from the morphologies of the tensile fracture that the fracture modes are more characterized by the cleavage cracking, so the plasticity and strength of the alloy are decreased, as shown in Fig. 7.

Since the grain of the 950°C specimen is finer than that of the 970°C specimen, the strength and elongation of the former are higher than those of the latter, but the differences are small, as shown in Fig. 7. On the one hand, due to the larger grain size of 970°C specimen, the plastic deformation coordination ability of the structure is reduced, which is not conducive to the improvement of strength and plasticity. On the other hand，the equiaxed α phase at the edge of the original particles is completely merged by the β phase as the specimen is HIPed in the β single-phase region. As a result, the adverse effect of the PPBs on the properties is completely eliminated, which is beneficial for the properties improvement. Thus, the combined effect of these two aspects makes similar tensile properties of the two specimens.

4.2. The effect of microstructure on the fracture toughness of the alloy

The strength and toughness of powder HIPed titanium alloys with different microstructures show completely different trends, as shown in Fig. 18. Theoretically, the fine-grained structure is conducive to improving the strength and toughness. In fact, strength and plasticity are the overall mechanical response controlled by the overall deformation of the alloy. Fracture toughness is the result of the mechanical response of the "local" microstructure deformation at the crack tip. The deformation area involved by the crack tip is many orders of magnitude smaller than the deformation in the tensile test. Therefore, the microstructure usually affects strength and toughness in different ways [7].

With the increase of the HIP temperature, the fracture toughness of specimens shows an increasing trend. Among them, the fracture toughness of specimens above 950°C has a significant increase. Lamellar structure is a very important factor affecting the fracture toughness of titanium alloys. It can be seen in Fig. 6 that the α lath spacing increases with the increase of HIP temperature. According to reports [26–31], by increasing α lath spacing, the size of the plastic zone at the tip of the crack can be increased to prevent further crack propagation. This provides important clues for analyzing the difference in fracture toughness of different specimens.

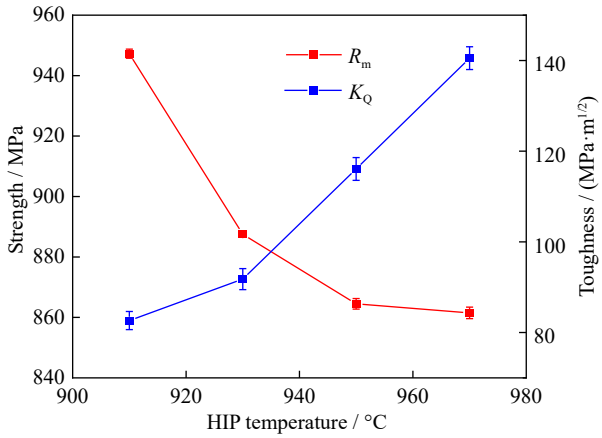

Fig. 18. Comparison of strength and toughness under different HIP temperatures.

The microstructure of the 910°C specimen and 930°C specimen consisted of equiaxed grain belts and lath clusters wrapped by the equiaxed grain belts. First, the PPBs in the equiaxed grain zone weaken the bonding strength of the structure. Debonding occurs under tensile stress and large-hole defects are generated, as shown in Fig. 13(c). For the specimen HIPed at 930°C, due to the increased diffusion bonding between powder particles, the influence of PPBs is weakened, and the proportion of pores is reduced. As a result, the toughness is improved. In addition, the plastic β phase undergoes plastic deformation under stress, and the surrounding ductile α phase plays a role in resisting plastic deformation. When the deformation of the β phase accumulates to a certain extent, it will debond from the α phase, thereby gathering linearly arranged micropores at the interface of the two phases, as shown in Figs. 13(d) and 14(d). These aggregated holes provide channels for crack propagation and accelerate the fracture process, thus the fracture toughness is reduced. According to literature reports [12,32], the fracture toughness of titanium alloys depends on the resistance to the growth of microcracks before unstable fracture to a large extent. When there are many defects in the structure, micropores are tend to form at these defects, causing cracking. This statement is consistent with the above analysis.

Specimens above 950°C are Widmanstatten structure or "near Widmanstatten structure" with a small amount of equiaxed α phase. Generally speaking, the fracture toughness of Widmanstatten structure is higher than that of other types of structure [17]. Through the analysis of the microstructure near the fracture surface, it is found that the 950°C and 970°C specimens have three kinds of toughening phenomena. Firstly, in the 950°C specimen, the propagation direction of the cracks is deflected when they encounter lath clusters with different orientations, as shown in Fig. 15(c). It can be seen from Fig. 16(d) that the fracture surface of the 970°C specimen is not smooth under the microscopic view, showing a saw-tooth-like morphology, indicating that the main crack has been deflected during the growth process. The continuous deflection of the crack propagation direction increases the tortuosity of the crack propagation path and the crack surface area, which plays a role in improving the toughness [17–20]. Secondly, it is found in Figs. 15(d) and 16(c) that the crack has undergone shear plastic deformation when it encounters the laths perpendicular to the crack direction. This is because the β phase in the lath structure is a plastic phase. When the crack propagates to this plastic phase, the local stress concentration at the crack tip is relaxed by shear de-

formation. At the same time, dispersive micropores are generated in the front edge of the crack tip, as shown by the red arrow in Figs. 15(d) and 16(c). According to the micro-crack-induced toughening mechanism, micro-crack nucleation occurs at the tip of the crack before unstable fracture, resulting in micro-holes, which can passivate the crack propagation, relax the stress concentration, and improve the toughness of the alloy [33–34]. Thirdly, crack bifurcation was found in the 970°C specimen, as shown in Fig. 16(b), forming new cracks parallel to the direction of the lath, which increases the tortuosity of the crack propagation path and the crack surface area [17,27,35–36]. This makes the fracture toughness of the 970°C alloy further increased. The α/β lamellar structure releases stress concentration through shear plastic deformation, and the wide and tough α laths force the crack to bifurcate and deflect, which has a positive effect on the crack propagation and improves the toughness. The microstructure with alternating two-phase lamellas exerts the toughening effect of composite structure.

In summary, fine-grain strengthening and composite structure toughening play a dominant role respectively in the specimens below 950°C and above 950°C. In order to improve the strength and toughness comprehensively, it is necessary to further adjust the range of HIP parameters to optimize the microstructure. Two possible ways are proposed. One is to eliminate the equiaxed grain belts in the "basket-like structure" structure to obtain a basket structure to eliminate PPBs and increase the spacing of the α laths appropriately. The other is to reduce the initial β grain size to obtain a fine-grained Widmanstatten structure.

5. Conclusions

In this paper, the effects of different microstructure characteristics on the strength, plasticity, and toughness of the powder HIPed TA15 alloy were investigated. The conclusions are as follows:

(1) The specimens HIPed below 950°C have fine-grained "basket-like structure," consisting of lath clusters and surrounding small equiaxed grains belts. With the increase of HIP temperature, the microstructure transforms into Widmanstatten structure, and the crystal grains increase significantly.

(2) The specimens HIPed below 950°C have higher strength and plasticity due to the strengthening effect of fine grains. As the HIP temperature increases, the strength and elongation of the alloy show a downward trend. The tensile strength and elongation are reduced from 948 MPa and 17.3% for the 910°C specimen to 861 MPa and 10% for the 970°C specimen. The corresponding tensile fracture mode changes from transcrystalline plastic fracture to mixed fracture including intercrystalline cleavage.

(3) The fracture toughness of the specimens increased from 82.64 $MPa \cdot m^{1/2}$ for the 910°C specimen to 140.18 $MPa \cdot m^{1/2}$ for the 970°C specimen. Specimens below 950°C tend to form holes due to PPBs, which is not conducive to toughening. Specimens above 950°C have high fracture toughness due to crack deflection, crack branching, and shear plastic deformation of the Widmanstatten structure.

Acknowledgements

This work was financially supported by the National Natural Science Foundation of China (Nos. 51874037 and 51922004), the Beijing Natural Science Foundation (No. 2212035), the Fundamental Research Funds for the Central Universities (No. FRF-TP-19005C1Z), and the National Defense Basic Research Project (No. JCKY2017213004).

Conflict of Interest

All authors have no financial/commercial conflicts of interest.

References

[1] L. Xu, R.P. Guo, Z.Y. Chen, Q. Jia, and Q.J. Wang, Mechanical property of powder compact and forming of large thin-wall cylindrical structure of Ti55 alloys, *Chin. J. Mater. Res.*, 30(2016), No. 1, p. 23.

[2] R. Baccino, F. Moret, F. Pellerin, D. Guichard, and G. Raisson, High performance and high complexity net shape parts for gas turbines: The ISOPREC® powder metallurgy process, *Mater. Des.*, 21(2000), No. 4, p. 345.

[3] Y. Pan, X. Lu, C.C. Liu, T.L. Hui, C. Zhang, and X.H. Qu, Sintering densification, microstructure and mechanical properties of Sn-doped high Nb-containing TiAl alloys fabricated by pressureless sintering, *Intermetallics*, 125(2020), art. No. 106891.

[4] X. Lu, Y. Pan, W.B. Li, M.D. Hayat, F. Yang, H. Singh, W.W. Song, X.H. Qu, Y. Xu, and P. Cao, High-performance Ti composites reinforced with *in situ* TiC derived from pyrolysis of polycarbosilane, *Mater. Sci. Eng. A*, 795(2020), art. No. 139924.

[5] X.H. Qu, G.Q. Zhang, and L. Zhang, Applications of powder metallurgy technologies in aero-engines, *J. Aeronaut. Mater.*, 34(2014), No. 1, p. 1.

[6] N.R. Moody, W.M. Garrison, J.E. Smugeresky, and J.E. Costa, The role of inclusion and pore content on the fracture toughness of powder-processed blended elemental titanium alloys, *Metall. Trans. A*, 24(1993), No. 1, p. 161.

[7] Y. Pan, W.B. Li, X. Lu, M.D. Hayat, L. Yin, W.W. Song, X.H. Qu, and P. Cao, Microstructure and tribological properties of titanium matrix composites reinforced with *in situ* synthesized TiC particles, *Mater. Charact.*, 170(2020), art. No. 110633.

[8] Y. Pan, W.B. Li, X. Lu, Y.C. Yang, Y.J. Liu, T.L. Hui, and X.H. Qu, Microstructure and mechanical properties of polycarbosilane *in-situ* reinforced titanium matrix composites, *Rare Met. Mater. Eng.*, 49(2020), No. 4, p. 1345.

[9] M.E. Launey and R.O. Ritchie, On the fracture toughness of advanced materials, *Adv. Mater.*, 21(2009), No. 20, p. 2103.

[10] C.S. Tan, Y.D. Fan, Q.Y. Sun, and G.J. Zhang, Improvement of the crack propagation resistance in an α + β titanium alloy with a trimodal microstructure, *Metals*, 10(2020), No. 8, art. No. 1058.

[11] M. Niinomi and T. Kobayashi, Fracture characteristics analysis related to the microstructures in titanium alloys, *Mater. Sci. Eng. A*, 213(1996), No. 1-2, p. 16.

[12] F. Cao, *Fatigue Behavior and Mechanisms in Powder Metallurgy Ti–6Al–4V Titanium Alloy* [Dissertation], The University

of Utah, Salt Lake City, 2016.
[13] H. Singh, M. Hayat, H.Z. Zhang, R. Das, and P. Cao, Effect of TiB_2 content on microstructure and properties of *in situ* Ti–TiB composites, *Int. J. Miner. Metall. Mater.*, 26(2019), No. 7, p. 915.
[14] L. Wang, Z.B. Lang, and H.P. Shi, Properties and forming process of prealloyed powder metallurgy Ti–6Al–4V alloy, *Trans. Nonferrous Met. Soc. China*, 17(2007), Suppl. 1, p. s639.
[15] A.A. Hidalgo, R. Frykholm, T. Ebel, and F. Pyczak, Powder metallurgy strategies to improve properties and processing of titanium alloys: A review, *Adv. Eng. Mater.*, 19(2017), No. 6, art. No. 1600743.
[16] J.W. Xu, W.D. Zeng, D.D. Zhou, H.Y. Ma, W. Chen, and S.T. He, Influence of alpha/beta processing on fracture toughness for a two-phase titanium alloy, *Mater. Sci. Eng. A*, 731(2018), p. 85.
[17] M. Niinomi and T. Kobayashi, Toughness and strength of microstructurally controlled titanium alloys, *ISIJ Int.*, 31(1991), No. 8, p. 848.
[18] X. Wen, M.P. Wan, C.W. Huang, and M. Lei, Strength and fracture toughness of TC21 alloy with multi-level lamellar microstructure, *Mater. Sci. Eng. A*, 740-741(2019), p. 121.
[19] R.P. Guo, L. Xu, J. Wu, R. Yang, and B.Y. Zong, Microstructural evolution and mechanical properties of powder metallurgy Ti–6Al–4V alloy based on heat response, *Mater. Sci. Eng. A*, 639(2015), p. 327.
[20] H.W. Wang, Z.J. Guo, and J. Wang, Study on microstructure and fracture toughness of TA15 alloy, *Rare Met. Mater. Eng.*, 34(2005), Suppl. 3, p. 293.
[21] H.E. Dève, A.G. Evens, and D.S. Shih, A high-toughness γ-titanium aluminide, *Acta Metall. Mater.*, 40(1992), No. 6, p. 1259.
[22] K. Zhang, J. Mei, N. Wain, and X. Wu, Effect of hot-isostatic-pressing parameters on the microstructure and properties of powder Ti–6Al–4V hot-isostatically-pressed samples, *Metall. Mater. Trans. A*, 41(2010), No. 4, p. 1033.
[23] C. Cai, B. Song, P.J. Xue, Q.S. Wei, C.Z. Yan, and Y.S. Shi, A novel near α-Ti alloy prepared by hot isostatic pressing: Microstructure evolution mechanism and high temperature tensile properties, *Mater. Des.*, 106(2016), p. 371.
[24] R.P. Guo, L. Xu, Z.Y. Chen, Q.J. Wang, B.Y. Zong, and R. Yang, Effect of powder surface state on microstructure and tensile properties of a novel near α-Ti alloy using hot isostatic pressing, *Mater. Sci. Eng. A*, 706(2017), p. 57.
[25] Q. Wang, Z. Wen, C. Jiang, B. Wang, and D.Q. Yi, Creep behaviour of TA15 alloy at elevated temperature, *Mater. Sci. Eng. Powder Metall.*, 19(2014), No. 2, p. 171.
[26] S.K. Li, S.X. Hui, W.J. Ye, Y. Yu, and B.Q. Xiong, Effects of microstructure on damage tolerance properties of TA15 ELI titanium alloy, *Chin. J. Nonferrous Met.*, 17(2007), No. 7, p. 1119.
[27] J.P. Hirth and F.H. Froes, Interrelations between fracture toughness and other mechanical properties in titanium alloys, *Metall. Trans. A*, 8(1977), No. 7, p. 1165.
[28] F.W. Chen, Y.L. Gu, G.L. Xu, Y.W. Cui, H. Chang, and L. Zhou, Improved fracture toughness by microalloying of Fe in Ti–6Al–4V, *Mater. Des.*, 185(2020), art. No. 108251.
[29] Z.F. Shi, H.Z. Guo, J.W. Zhang, and J.N. Yin, Microstructure–fracture toughness relationships and toughening mechanism of TC21 titanium alloy with lamellar microstructure, *Trans. Nonferrous Met. Soc. China*, 28(2018), No. 12, p. 2440.
[30] A. Ghosh, S. Sivaprasad, A. Bhattacharjee, and S.K. Kar, Microstructure–fracture toughness correlation in an aircraft structural component alloy Ti–5Al–5V–5Mo–3Cr, *Mater. Sci. Eng. A*, 568(2013), p. 61.
[31] N.L. Richards, Quantitative evaluation of fracture toughness–microstructural relationships in alpha–beta titanium alloys, *J. Mater. Eng. Perform.*, 13(2004), No. 2, p. 218.
[32] X.H. Shi, W.D. Zeng, and Q.Y. Zhao, The effects of lamellar features on the fracture toughness of Ti-17 titanium alloy, *Mater. Sci. Eng. A*, 636(2015), p. 543.
[33] T. Horiya, H.G. Suzuki, and T. Kishi, Effect of microstructure and impurity content on microcrack initiation and extension properties of Ti–6Al–4V alloys, *Tetsu-to-Hagane*, 75(1989), No. 12, p. 2250.
[34] Y. Kawabe and S. Muneki, Strengthening and toughening of titanium alloys, *ISIJ Int.*, 31(1991), No. 8, p. 785.
[35] N.L. Richards, Prediction of crack deflection in titanium alloys with a platelet microstructure, *J. Mater. Eng. Perform.*, 14(2005), No. 1, p. 91.
[36] Q.L. Zhang and X.W. Li, Effect of structure on fatigue properties and fracture toughness for TA15 titanium alloy, *J. Mater. Eng.*, 2007, No. 7, p. 3.